

Climatology of oceanic coherent eddies

Josué Martínez-Moreno¹, Andrew McC. Hogg¹, and Matthew H. England²

¹Research School of Earth Science and ARC Center of Excellence for Climate Extremes, Australian National University, Canberra, Australia

²Climate Change Research Centre (CCRC), UNSW Australia, Sydney NSW, Australia

Key Points:

- Coherent eddies contain around 50% of the surface ocean kinetic energy budget.
- Seasonal cycle of the number of coherent eddies and coherent eddy amplitude reveal a 3-6 month lag to wind forcing.
- The seasonal lag between the number and the amplitude of coherent eddies suggests a role for the inverse cascade.

Corresponding author: Josué Martínez-Moreno, josue.martinezmoreno@anu.edu.au

12 **Abstract**

13 Ocean eddies influence regional and global climate through mixing and transport of heat
 14 and properties. One of the most recognizable and ubiquitous feature of oceanic eddies
 15 are coherent vortices with spatial scales of tens to hundreds of kilometers, frequently re-
 16 ferred as “mesoscale eddies”. Coherent mesoscale eddies are known to transport prop-
 17 erties across the ocean and to locally affect near-surface wind, cloud properties and rain-
 18 fall patterns. Although coherent eddies are ubiquitous, their climatology, seasonality and
 19 long-term temporal evolution remains poorly understood. Thus, we examine the kinetic
 20 energy contained by coherent eddies and present the seasonal, inter-annual and long-term
 21 variability of automatically identified coherent eddies from satellite observations from
 22 1993 to 2019. Around 50% of the kinetic energy contained by ocean eddies corresponds
 23 to coherent eddies. Additionally, a strong seasonal cycle is observed, with a 3–6 months
 24 lag between the wind forcing and the response of the coherent eddy field. The season-
 25 ality of the number of coherent eddies and their amplitude reveals that the number of
 26 coherent eddies responds faster to the forcing (~ 3 months), than the coherent eddy am-
 27 plitude (which is lagged by ~ 6 months). Our analysis highlights the relative importance
 28 of the coherent eddy field in the ocean kinetic energy budget, implies a strong response
 29 of the eddy number and eddy amplitude to forcing at different time-scales, and show-
 30 cases the seasonality, and multidecadal trends of coherent eddy properties.

31 **Plain language summary**

32 Coherent eddies are the most common feature in the oceans observable from satel-
 33 lites. They are crucial in ocean dynamics as they can transport properties over long dis-
 34 tances and interact with the atmosphere. Our study investigates the seasonal and long-
 35 term changes in the abundance and intensity of coherent eddies, by automatically iden-
 36 tifying individual eddies over the satellite altimeter record. The seasonal cycle suggests
 37 a transition from numerous, smaller, and weaker coherent eddies, to fewer and larger,
 38 and stronger coherent eddies over the season. In addition, a long-term adjustment of the
 39 coherent eddy field is identified possible due to long-term changes in the climate system.

40 **1 Introduction**

41 Mesoscale ocean variability with spatial scales of tens to hundreds of kilometers is
 42 comprised of processes such as vortices, waves, and jets (Ferrari & Wunsch, 2009; Fu et

43 al., 2010). These mesoscale processes are highly energetic, and they play a crucial role
 44 in the transport of heat, salt, momentum, and other tracers through the ocean (Wun-
 45 sch & Ferrari, 2004; Wyrtki et al., 1976; Gill et al., 1974). Possibly, the most recogniz-
 46 able and abundant process observed from satellites is mesoscale vortices. Although mesoscale
 47 vortices are commonly referred to in literature as “mesoscale eddies”, this term is also
 48 often used to describe the total mesoscale ocean variability (the time-varying component
 49 of the mesoscale flow), thus, here we will refer to mesoscale vortices as *coherent eddies*.

50 Coherent eddies are quasi-circular geostrophic currents. According to their rota-
 51 tional direction, the sea surface height anomaly within a coherent eddy can have a neg-
 52 ative or positive sea surface height anomaly (cold-core and warm-core coherent eddies,
 53 respectively). This characteristic sea surface height signature of coherent eddies has been
 54 utilized to automatically identify and track coherent eddies from satellite altimetry (Chel-
 55 ton et al., 2007; Faghmous et al., 2015; Ashkezari et al., 2016; Martínez-Moreno et al.,
 56 2019; Cui et al., 2020). Automated identification algorithms of coherent eddies have shown
 57 their ubiquity in the oceans, with a predominant influence at hotspots of eddy activity
 58 such as boundary extensions and the Antarctic Circumpolar Current. In these regions,
 59 Chelton et al. (2011) estimated that coherent eddies contribute around 40–50% of the
 60 mesoscale kinetic energy (Chelton et al., 2011) and thus a significant fraction of the to-
 61 tal kinetic energy (Ferrari & Wunsch, 2009). Although this unique estimate showcases
 62 the importance of the mesoscale coherent eddy field, the energy contained by coherent
 63 eddies was estimated by extracting the total geostrophic velocity within the radius of
 64 each detected coherent eddy; thus, it is possible that this estimate may contain energy
 65 from other processes. Coherent eddies are abundant and energetic; therefore they are
 66 also essential to ocean dynamics as concluded by many previous studies (Hogg & Blun-
 67 dell, 2006; Siegel et al., 2011; Beron-Vera et al., 2013; Frenger et al., 2013, 2015; Pilo et
 68 al., 2015; Schubert et al., 2019; Patel et al., 2020).

69 There is broad consensus that mesoscale eddy kinetic energy has a pronounced sea-
 70 sonal variability (Qiu, 1999; Qiu & Chen, 2004; Kang & Curchitser, 2017; Uchida et al.,
 71 2017). Several hypotheses have been proposed to explain this seasonality including: sea-
 72 sonal variations of atmospheric forcing (Sasaki et al., 2014), seasonality of the mixed layer
 73 depth (Qiu et al., 2014; Callies et al., 2015), seasonality of the intensity of barotropic in-
 74 stability (Qiu & Chen, 2004), the variability of the baroclinic instability due to the sea-
 75 sonality of the vertical shear (Qiu, 1999), and a seasonal lag of the inverse energy cas-

76 cade (i.e. energy is transported between scales, from small to large; Arbic et al., 2013)
 77 in combination with the presence of a front in the mixed layer, which can lead to a sea-
 78 sonal cycle of the baroclinic instability (Qiu et al., 2014). On one hand, processes such
 79 as barotropic and baroclinic instabilities control the seasonality of coherent eddies in the
 80 ocean. On the other hand, recent studies using observations and eddy-permitting climate
 81 models suggest several long-term adjustments of the global ocean capable of long-term
 82 changes in the coherent eddy field. Such readjustments include a multidecadal increase
 83 in the ocean stratification resulted from temperature and salinity changes (Li et al., 2020),
 84 a horizontal readjustment of the sea surface temperature gradients (Cane et al., 1997; Bouali
 85 et al., 2017; Ruela et al., 2020), and an intensification of the kinetic energy, eddy kinetic
 86 energy, and mesoscale eddy kinetic energy over the last 3 decades as a consequence of
 87 an increase in wind forcing (Hu et al., 2020; Wunsch, 2020; Martínez-Moreno et al., 2021).
 88 All these seasonal factors and long-term readjustments directly influence the annual and
 89 decadal response of the coherent eddy field, however, the seasonality of the coherent com-
 90 ponent of the eddy kinetic energy, as well as the seasonal cycle and trends of the coher-
 91 ent eddy statistics remain unknown.

92 Here we present a new global climatology of the coherent eddy kinetic energy by
 93 reconstructing the coherent eddy signature from satellite observations. Our study doc-
 94 uments the seasonal cycle of the coherent eddy kinetic energy, and the seasonal cycle and
 95 long-term trends of the coherent eddy properties over the satellite record. Moreover, we
 96 conduct more detailed analyses in regions where coherent eddies dominate the eddy ki-
 97 netic energy field. This paper is structured as follows: the data sources and methodol-
 98 ogy are described in section 2. Then, we present the climatology, energy ratios, and global
 99 seasonality of the coherent eddy kinetic energy in section 3. Section 4 outlines the global
 100 climatology and seasonality of coherent eddy properties, followed by long-term changes
 101 of the coherent eddy properties (section 5). Then we focus our attention on the seasonal
 102 cycle and coherent eddy properties in regions dominated by coherent eddies (section 6).
 103 Finally, section 7 summarizes the main results and discusses the implications of this study.

104 2 Methods

105 We use daily sea surface height (SSH) data made available by the Copernicus Ma-
 106 rine Environment Monitoring Service in near real time (CMEMS, 2017). This gridded
 107 product contains the sea surface height and geostrophic velocities with daily 0.25° res-

108 olution from January 1993 to 2019. The daily geostrophic velocities allowed us to com-
 109 pute the kinetic energy (KE) and eddy kinetic energy (EKE) over the satellite record.
 110 The main source of EKE is the time-varying wind (Ferrari & Wunsch, 2009), thus we
 111 computed the seasonal cycle of the wind magnitude from the JRA55 reanalysis (Japan
 112 Meteorological Agency, Japan, 2013) using wind velocities at 10m above the ocean's sur-
 113 face.

114 Over the same record, coherent eddy statistics from Martínez-Moreno et al. (2019),
 115 hereafter MM19, are analyzed and compared with those released by Chelton & Schlax
 116 (2013). Both datasets are gridded in a 1° resolution and are produced via automated
 117 eddy identification algorithms using closed contours of SSH. However, these datasets have
 118 important differences in the criteria they use to identify and record coherent eddies statis-
 119 tics. The major differences include: (i) MM19's algorithm requires an adjustment be-
 120 tween a 2D Gaussian and the SSH anomaly (SSHa) surface within the identified closed
 121 contour, while Chelton's only uses the outer-most closed contour of SSH; (ii) MM19's
 122 dataset reports the maximum SSHa within the identified coherent eddy, while Chelton's
 123 algorithm reports the maximum SSH value minus the discrete level in which the coher-
 124 ent eddy was identified; MM19's dataset includes all detected coherent eddies, while Chel-
 125 ton's dataset excludes (iii) coherent eddies with lifetimes shorter than four weeks and
 126 (iv) coherent eddy amplitudes smaller than 1cm. Moreover, MM19's algorithm allows
 127 the reconstruction of the coherent eddy field under the assumption that coherent eddies
 128 have a 2D Gaussian imprint in the sea surface height. This Gaussian reconstruction of
 129 the coherent eddy field then allowes us to estimate the coherent geostrophic eddy veloc-
 130 ities and thus the kinetic energy contained only by coherent eddies.

131 2.1 Kinetic Energy decomposition

132 Kinetic energy is commonly divided into the mean and time-varying components
 133 through a Reynolds decomposition. At a given time, the surface velocity field $\mathbf{u} = (u, v)$
 134 is split into the time mean ($\bar{\mathbf{u}}$) and time varying components (\mathbf{u}'). Moreover, MM19 pro-
 135 posed to further decompose the eddy kinetic energy into the energy contained by coher-
 136 ent features (\mathbf{u}_e') and non-coherent features (\mathbf{u}_n'). Therefore the KE equation can be writ-
 137 ten as:

$$\text{KE} = \underbrace{\bar{u}^2 + \bar{v}^2}_{\text{MKE}} + \underbrace{\underbrace{u_e'^2 + v_e'^2}_{\text{CEKE}} + \underbrace{u_n'^2 + v_n'^2}_{\text{nCEKE}}}_{\text{EKE}} + \mathcal{O}_c^2 + \mathcal{O}^2 \quad (1)$$

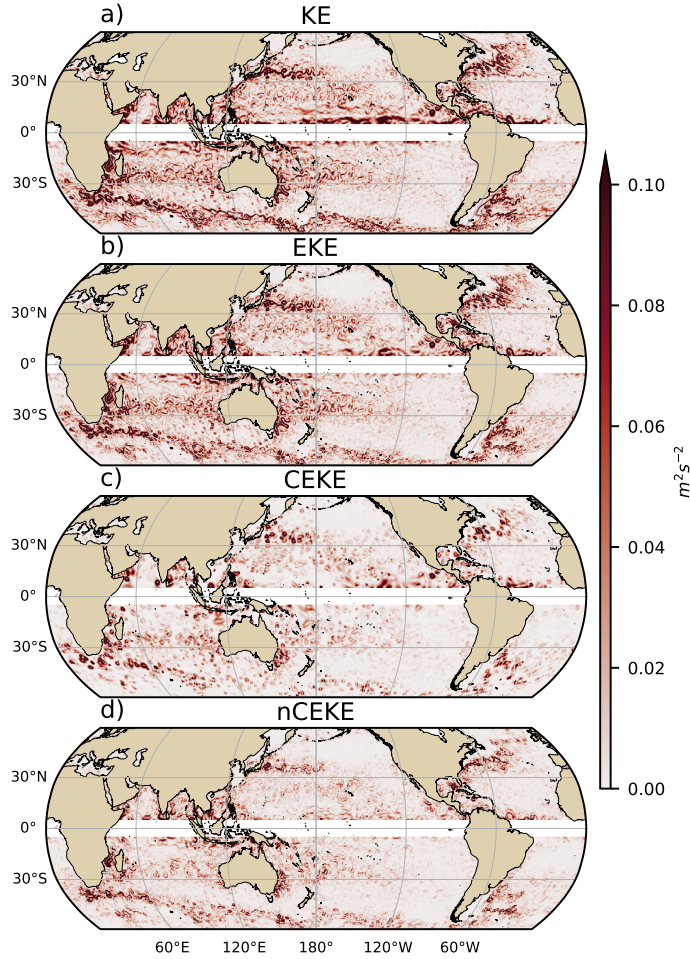
138 Due to the properties of this decomposition, the second order term \mathcal{O}^2 is zero when
 139 averaged over the same period as $\bar{\mathbf{u}}$. However, \mathcal{O}_c^2 is not necessarily negligible, unless it
 140 is averaged over time and space. More information about the decomposition of the field
 141 into coherent features and non-coherent features is explained by Martínez-Moreno et al.
 142 (2019). A global snapshot of each component of kinetic energy decomposition is shown
 143 in Figure 1, where the KE and EKE are comprised of rings and filaments. As expected,
 144 the decomposition of EKE into CEKE and nCEKE components exhibit only ring-like
 145 signatures expected of coherent eddies, while the non-coherent component shows primarily
 146 filaments with some mis-identified coherent eddies.

150 2.2 Eddy statistics

151 The eddy statistics used in this study include (i) the eddy count ($c\text{Eddy}_n$) defined
 152 as the number of eddies per grid cell, (ii) the eddy diameter defined as the diameter of
 153 a circle with equal area to the closed contour of each identified eddy, and (iii) the mean
 154 eddy amplitude defined as the mean amplitude of the coherent eddies within the cell ($c\text{Eddy}_{amp}$).
 155 The latter metric can be separated into positive ($c\text{Eddy}_{amp}^+$) and negative ($c\text{Eddy}_{amp}^-$)
 156 coherent eddy amplitudes, defined as the mean amplitude of warm core and cold core
 157 coherent eddies, respectively, within the cell. The polarity independent eddy amplitude
 158 ($|c\text{Eddy}_{amp}|$) is defined as:

$$|c\text{Eddy}_{amp}| = \frac{1}{2} (c\text{Eddy}_{amp}^+ - c\text{Eddy}_{amp}^-) \quad (2)$$

159 Note that the $c\text{Eddy}_{amp}^+$ and $c\text{Eddy}_{amp}^-$ are sign definite, thus the difference will always
 160 be positive, the gridded averaged $c\text{Eddy}_{amp}$ can be negative or positive noting the dom-
 161 inant polarity of coherent eddies in the region, and the absolute $c\text{Eddy}_{amp}$ is denoted
 162 by $c\text{Eddy}_{|amp|}$. We analyze the climatology and trends of the eddy statistics between
 163 1993 and 2019. We exclude the equatorial region (10°S - 10°N) and regions poleward
 164 of 60° . Note that the climatology of $c\text{Eddy}_n$ is computed by adding all the identified ed-
 165 dies over the record, while all other climatological statistics are computed as the time-
 166 average over the record. Seasonal climatologies are calculated for the monthly average
 167 of each coherent eddy statistic, while hemispherical time-series are filtered with a run-



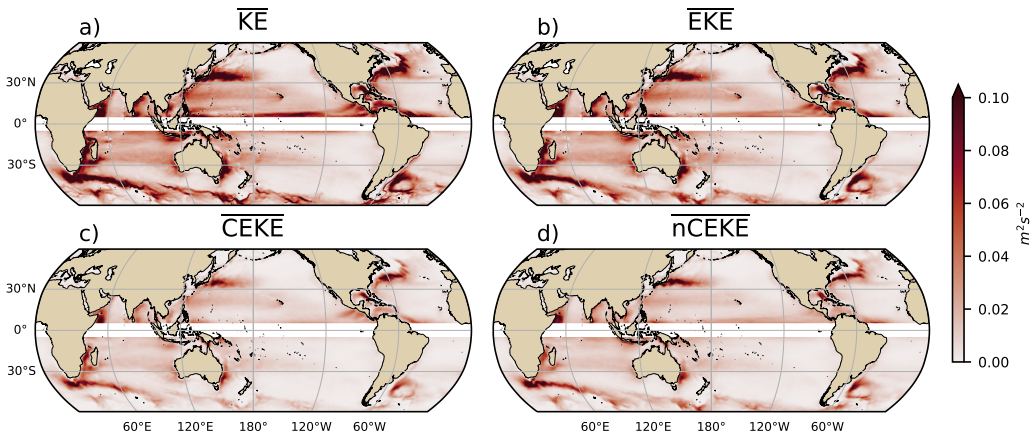
147 **Figure 1.** Snapshot of surface kinetic energy (\bar{KE}), surface eddy kinetic energy (\bar{EKE}),
 148 surface coherent eddy kinetic energy (\bar{CEKE}), and surface non-coherent eddy kinetic energy
 149 (\bar{nCEKE}) for the 1st of January 2017.

168 ning average of 90 days. Trends of $cEddy_n$ and $|cEddy_{amp}|$ are calculated by coarsen-
 169 ing the dataset to a 5° grid, and then linear trends are computed for each grid point, the
 170 statistical significance is assessed by a modified Mann-Kendall test (Yue & Wang, 2004).

171 Time averages are denoted by $\overline{\cdot}$, while area-weighted averages are denoted using
 172 $\langle \cdot \rangle$, the area-weighted of function f is:

$$\langle f \rangle = \frac{\int f \xi dx dy}{\int \xi dx dy}, \quad (3)$$

173 Where ξ is a mask that is set to zero in grid cells where no coherent eddies were iden-
 174 tified.

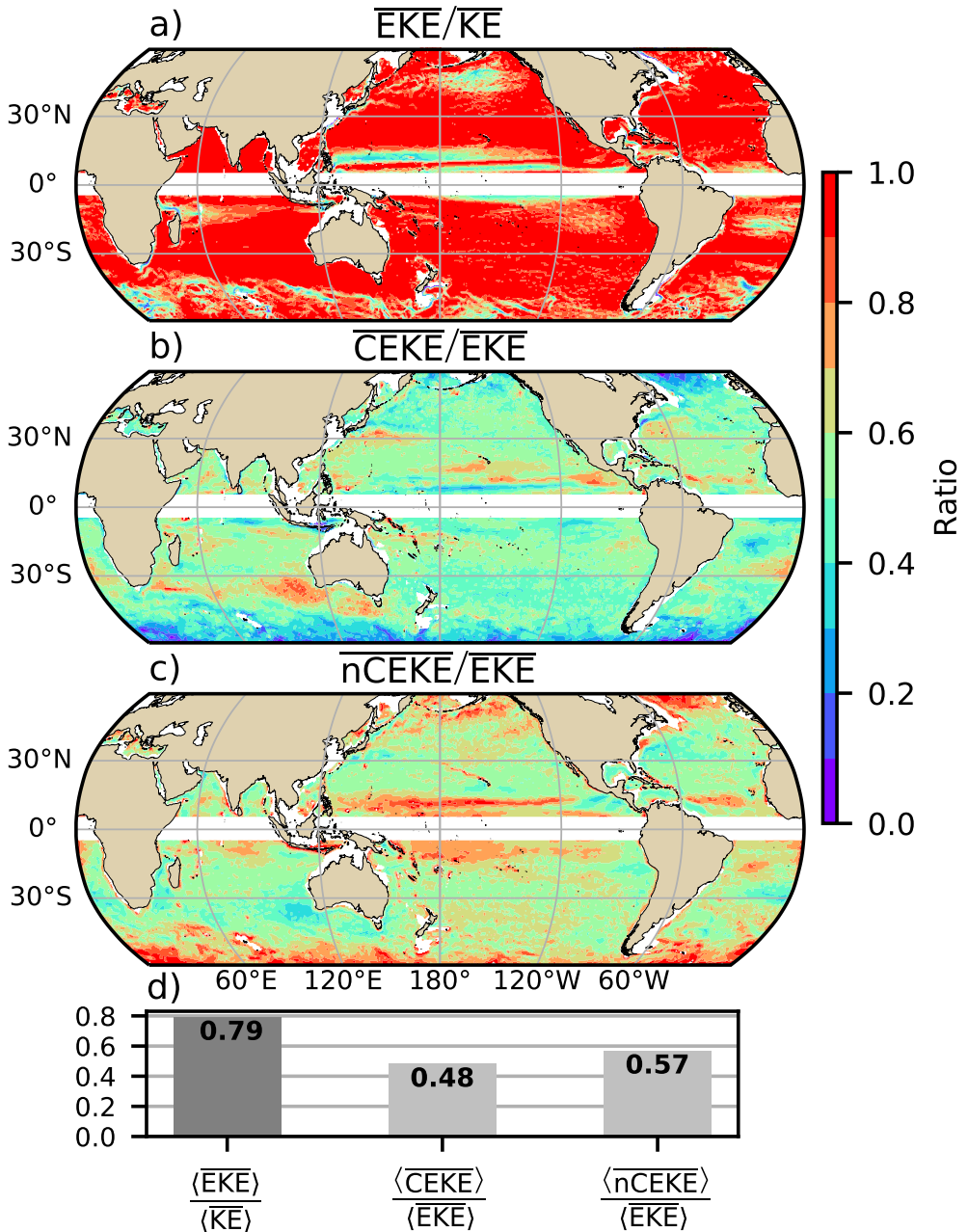


188 **Figure 2.** Mean surface kinetic energy (\overline{KE}), surface eddy kinetic energy (\overline{EKE}), surface coherent eddy kinetic energy (\overline{CEKE}), and surface non-coherent eddy kinetic energy (\overline{nCEKE})
189 between 1993-2018.
190

175 3 Global Coherent Eddy Energetics

176 The kinetic energy decomposition estimated from sea surface height measured by
177 satellite altimeters averaged from 1993-2019 is shown in Figure 2. These maps show that
178 many regions of the global ocean are highly energetic in mean KE (\overline{KE}), mean EKE (\overline{EKE}),
179 mean coherent eddy kinetic energy (\overline{CEKE}) and mean non-coherent eddy kinetic energy
180 (\overline{nCEKE}). The spatial pattern highlights well-known regions of the ocean where mesoscale
181 processes are abundant, such as the western boundary extensions and the Antarctic Cir-
182 cumpolar Current. The spatial distribution of the energy contained by the reconstructed
183 mesoscale coherent eddies and non-coherent components are similar (Figures 2c,d). How-
184 ever, there are some regions where coherent eddies dominate over non-coherent, and vice-
185 versa. Overall, this decomposition suggest that boundary current extensions and other
186 energetic regions, in particular, eddy-rich regions in the ocean contain both coherent
187 and non-coherent components of the kinetic energy.

200 Eddy kinetic energy is known to be more than an order of magnitude greater than
201 kinetic energy of the mean flow (MKE; Gill et al. 1974); this result is clearly shown in
202 Figure 3a, where \overline{EKE} is responsible for almost all the \overline{KE} across the ocean, except for
203 regions with persistent currents over time. Such regions are located in the mean bound-
204 ary extension locations, the equatorial Pacific currents and regions in the Antarctic Cir-
205 cumpolar Current, where the \overline{EKE} explains around 40% of the \overline{KE} . In a previous study,



191 **Figure 3.** Ratios of the kinetic energy components. a) Map of the proportion of mean eddy
 192 kinetic energy (\overline{EKE}) versus mean kinetic energy (\overline{KE}); b) Map of the percentage of mean co-
 193 herent eddy kinetic energy (\overline{CEKE}) versus mean eddy kinetic energy (\overline{EKE}); c) Map of the
 194 percentage of mean non-coherent eddy kinetic energy (\overline{nCEKE}) versus mean eddy kinetic energy
 195 (\overline{EKE}); d) Global time and area averaged (represented by $\langle \rangle$) percentage of mean eddy kinetic
 196 energy ($\langle \overline{EKE} \rangle$) versus the global mean kinetic energy ($\langle \overline{KE} \rangle$), area averaged percentage of mean
 197 coherent eddy kinetic energy ($\langle \overline{CEKE} \rangle$) and mean non coherent eddy kinetic energy ($\langle \overline{nCEKE} \rangle$)
 198 versus global mean eddy kinetic energy ($\langle \overline{EKE} \rangle$). Regions where the depth of the ocean is shall-
 199 lower than 1000m are removed from the ratio estimation.

Chelton et al. (2011) estimated that the EKE within coherent eddies with lifetimes greater than 4 weeks contain between 40 to 60 percent of the $\overline{\text{EKE}}$. Our method to reconstruct the coherent eddy signature (Figure 3b) further corroborates that the coherent component ($\langle \overline{\text{CEKE}} \rangle$) has $\sim 48\%$ of the $\langle \overline{\text{KE}} \rangle$ (Figure 3d). Furthermore, global area averages of the ratios show $\langle \overline{\text{EKE}} \rangle$ explains $\sim 78\%$ of the ocean $\langle \overline{\text{KE}} \rangle$ field, while non coherent eddy features contain $\sim 57\%$ percent of the $\langle \overline{\text{EKE}} \rangle$. Note the globally averaged coherent and non coherent components do not add to 100% as the cross terms (\mathcal{O}_c^2) are non-zero and coherent eddy reconstruction errors. The spatial pattern reveals a dominance of the $\overline{\text{CEKE}}$ equatorward from the boundary extensions and areas with large coherent eddy contributions of around 80% of the region's eddy kinetic energy can be found south of Australia, the Tehuantepec Gulf, and the tropical Atlantic. An evident signal is a reduction of the energy contained by coherent eddies at high latitudes and an increase in the energy explained by non-coherent eddies; this signal could be a consequence of the inability of the 0.25° satellite resolution (~ 13 km at 60°) to resolve coherent eddies with scales smaller than ~ 10 km (first baroclinic Rossby radius at 60° ; Chelton et al. 1998).

Figure 4 shows the seasonal cycle of the area weighted EKE and CEKE for the Northern Hemisphere ($\langle \text{EKE} \rangle_{NH}$ and $\langle \text{CEKE} \rangle_{NH}$; $10^\circ\text{N} - 60^\circ\text{N}$) and Southern Hemisphere ($\langle \text{EKE} \rangle_{SH}$ and $\langle \text{CEKE} \rangle_{SH}$; $60^\circ\text{S} - 10^\circ\text{S}$). In both hemispheres, the $\langle \text{EKE} \rangle$ and $\langle \text{CEKE} \rangle$ peak during summer. In the Northern Hemisphere, the largest $\langle \text{EKE} \rangle_{NH}$ and $\langle \text{CEKE} \rangle_{NH}$ occurs in July, ~ 6 months after the maximum winds in January (purple bar and back star in Figure 4c and d). Meanwhile, the Southern Ocean $\langle \text{EKE} \rangle_{SH}$ and $\langle \text{CEKE} \rangle_{SH}$ seasonal maxima arises during December, ~ 4 months after the maximum winds in August (purple bar and back star in Figure 4g, and h). This lag between winds and the eddy and coherent eddy energy components is further discussed in section 4.

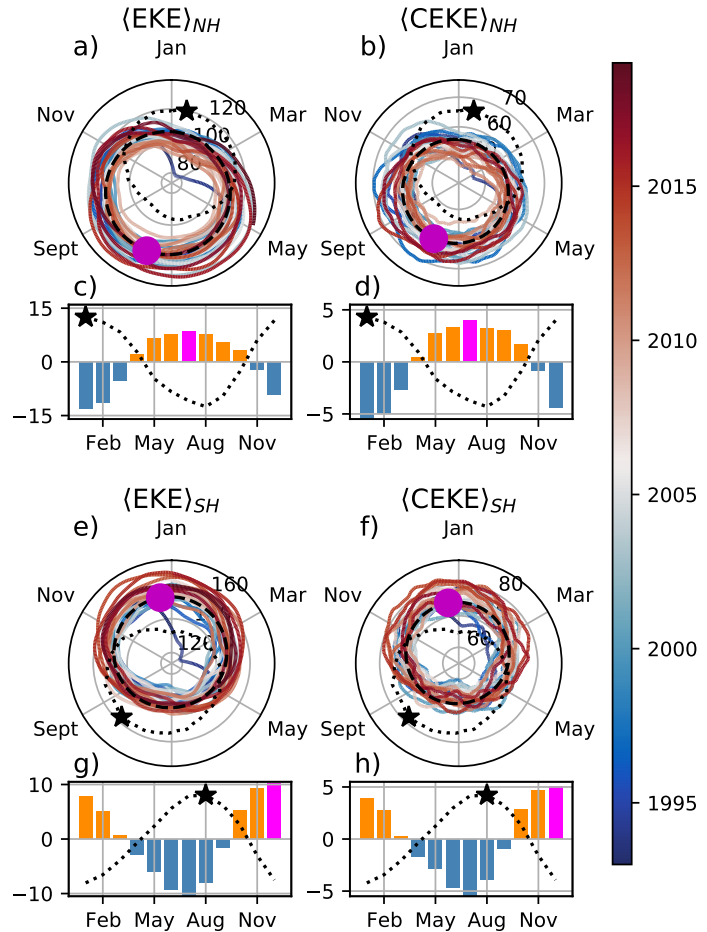
The cyclic plots in Figure 4 show the temporal evolution of $\langle \text{EKE} \rangle$ and $\langle \text{CEKE} \rangle$. Note that high frequency variability can be observed in the $\langle \text{CEKE} \rangle$ field with temporal scales of a few months, this variability could be attributed local dynamics averaged over the hemisphere, as well as errors within the coherent eddy reconstruction. Additionally, concentric changes in the cyclic plots highlight long-term changes over the record. For example, the Northern Hemisphere winters in early years of the record (blue) had a more energetic coherent eddy field, which has transitioned to weaker coherent energy contents since 2010 (red), in other words, the intensity of the $\langle \text{CEKE} \rangle_{NH}$ field has decreased. A larger long-term change can be observed in the Southern Hemisphere, where

239 concentric growth over time in $\langle \text{EKE} \rangle_{SH}$ and $\langle \text{CEKE} \rangle_{SH}$ support the previously observed
 240 strengthening of the eddy field in the Southern Ocean (Hogg et al., 2015; Martínez-Moreno
 241 et al., 2019; Martínez-Moreno et al., 2021).

251 4 Global Coherent Eddy Statistics

252 Coherent eddy kinetic energy allows us to quantify and study the energy of the eddy
 253 field, but the coherent eddy properties computed by automated coherent eddy identi-
 254 fication algorithms allow us investigate in more detail the contribution and temporal changes
 255 of their abundance (the number of eddies) and their intensity (both their amplitude and
 256 diameter). Figure 5 shows gridded climatologies of the number of eddies and the eddy
 257 amplitude. We contrast our MM19 eddy count with Chelton et al. (2007) (Figure 5a-
 258 b). Although the number of the identified eddies is larger in MM19, possibly due to the
 259 lifespan filter implemented by Chelton, both datasets reveal consistent spatial patterns.
 260 For example, both datasets show high abundance of eddies in the East North Pacific,
 261 East North Atlantic, as well as the East South Pacific, East South Atlantic and East In-
 262 dian Ocean, and small number counts of eddies in the tropics and in high latitudes ($\sim 60^\circ$).
 263 An interesting pattern also emerges in both eddy count datasets, where small scale struc-
 264 tures emerge in the eddy count field. These small structures highlight preferential co-
 265 herent eddy paths observable in boundary extensions and regions in the Southern Ocean.
 266 These structures and paths of coherent eddies could be associated with topographic fea-
 267 tures, however they remain a puzzling consistency between the eddy count pattern us-
 268 ing these two eddy identification methods.

274 Regions with large counts of eddies have in general small absolute amplitudes (Fig-
 275 ure 5 c), ocean gyre interiors follow with a larger absolute amplitude and finally regions
 276 such as the boundary extensions and Antarctic Circumpolar Current have the largest
 277 coherent eddy absolute amplitudes as shown by Chelton et al. (2011). Eddy amplitude
 278 highlights regions dominated by a given coherent eddy polarity, for example, boundary
 279 extensions have a preferred sign (Figure 5 d); positive amplitude polewards of the bound-
 280 ary extension mean location, and negative amplitude equatorwards. This sign preference
 281 is consistent with the preferential way coherent eddies are shed from boundary exten-
 282 sions; warm core eddies (positive) polewards of the boundary current extension, and equa-
 283 torward for cold core eddies (negative) (Kang & Curchitser, 2013; Chelton et al., 2011,
 284 2007). These global statistics reveal the absolute coherent eddy amplitude is a proxy for



242 **Figure 4.** Seasonality of the area-weighted eddy kinetic energy ($\langle EKE \rangle$), coherent eddy ki-
 243 netic energy ($\langle CEKE \rangle$). Panels a and b show the time-series of the Northern Hemisphere, while
 244 panels e and f correspond to the Southern Hemisphere. Panels c and d show the seasonal cycle of
 245 the $\langle EKE \rangle_{NH}$ and $\langle CEKE \rangle_{NH}$ in the Northern Hemisphere, and panels g and h show the South-
 246 ern Hemisphere ($\langle EKE \rangle_{SH}$ and $\langle CEKE \rangle_{SH}$). Dashed lines correspond to the seasonal cycle of the
 247 fields and dotted lines show the seasonal cycle of the wind magnitude smoothed over 120 days
 248 (moving average). The black and magenta markers (circle and bar) show the maximum of the
 249 seasonal cycle for the kinetic energy components and the wind magnitude, respectively. In cyclic
 250 plots, line colors shows the year.

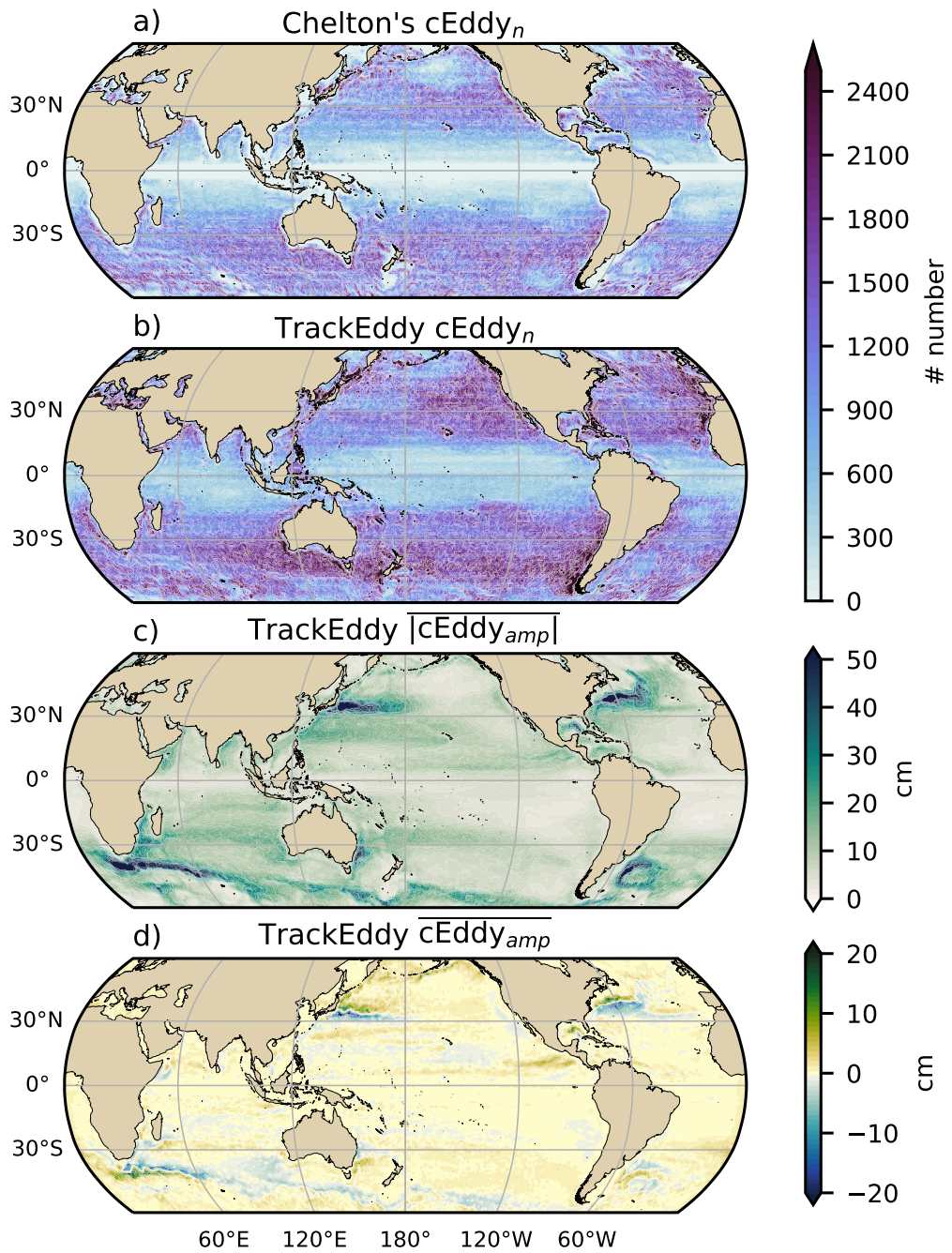


Figure 5. Averaged coherent eddy statistics. a) Climatology of the number of coherent eddies ($cEddy_n$) identified by Chelton et al. (2007); b) Climatology of the number of coherent eddies ($cEddy_n$) identified by Martínez-Moreno et al. (2019); c) Climatology of the mean absolute coherent eddy amplitude ($cEddy_{amp}$). d) Climatology of the mean coherent eddy amplitude ($cEddy_{amp}$).

285 the CEKE with similar spatial patterns (Figure 2 & Figure 5 c) and showcases that re-
 286 gions where $\overline{\text{CEKE}}$ has a large proportion of $\overline{\text{EKE}}$ (Figure 3), the absolute coherent eddy
 287 amplitude is also large.

288 To further understand the seasonal cycle of $\langle \text{CEKE} \rangle$, we compute the climatology
 289 of coherent eddy properties in each hemisphere (Figure 6). The seasonality of the num-
 290 ber of eddies in the Northern Hemisphere peaks on April (Figure 6 a, c), while the South-
 291 ern Hemisphere maximum number of eddies occurs during October (Figure 6 e, g). Mean-
 292 while, the seasonality of the eddy amplitude ($\langle |c\text{Eddy}_{amp}| \rangle$) peaks in August and Jan-
 293 uary for the Northern and Southern Hemispheres respectively (Figure 6 b, d, f, and h).
 294 As expected, the seasonality of $\langle |c\text{Eddy}_{amp}| \rangle$, or equivalent to the intensity of the co-
 295 herent eddies, is consistent with the seasonal cycle of $\langle \text{CEKE} \rangle$.

296 A key feature of Figure 6 is a distinct lag of ~ 3 months between the winds and eddy
 297 count, while the eddy amplitude maximum occurs ~ 6 months after the seasonal max-
 298 ima in winds. We suggest that the eddy number increases earlier in the year and, through
 299 eddy-eddy interactions (merging of coherent eddies), the amplitude of the coherent eddy
 300 increases ~ 3 months after. This seasonal lag and summer maxima is consistent with pre-
 301 vious studies which suggest that a time-lag of the inverse cascade (Sasaki et al., 2014;
 302 Qiu et al., 2014) is responsible of the EKE seasonal cycle, where winter has the highest
 303 energy at the smallest scales (non-resolvable with satellite observations), spring and au-
 304 tumn have the highest and lowest energy in scales of 50-100 km, and summertime has
 305 the highest energy at the largest scales (> 100 km; Uchida et al. 2017). Thus, the max-
 306 imum of $\langle \text{EKE} \rangle$, $\langle \text{CEKE} \rangle$, and $\langle |c\text{Eddy}_{amp}| \rangle$ located during summertime suggest that
 307 the seasonality of eddies and coherent eddies could be dominated by scales larger than
 308 100 km.

309 This result can be further explored by looking at the seasonal evolution of the eddy
 310 diameter ($c\text{Eddy}_d$). Note that 90% of identified coherent eddies have diameters between
 311 50 to 220 km (Figure 7 a). We divided eddies into large-scale coherent eddies (diam-
 312 ter > 120 km) and small-scale coherent eddies (diameter < 120 km; Figure 7a). In the
 313 Northern Hemisphere, small eddies have a seasonal peak in diameter during May, while
 314 large eddies have the greatest diameter in September (Figure 7 b). Meanwhile, in the
 315 Southern Hemisphere, the small-scale coherent eddies have the maximum diameter in
 316 December, while large-scale coherent eddies peak in February (Figure 7 c). This result

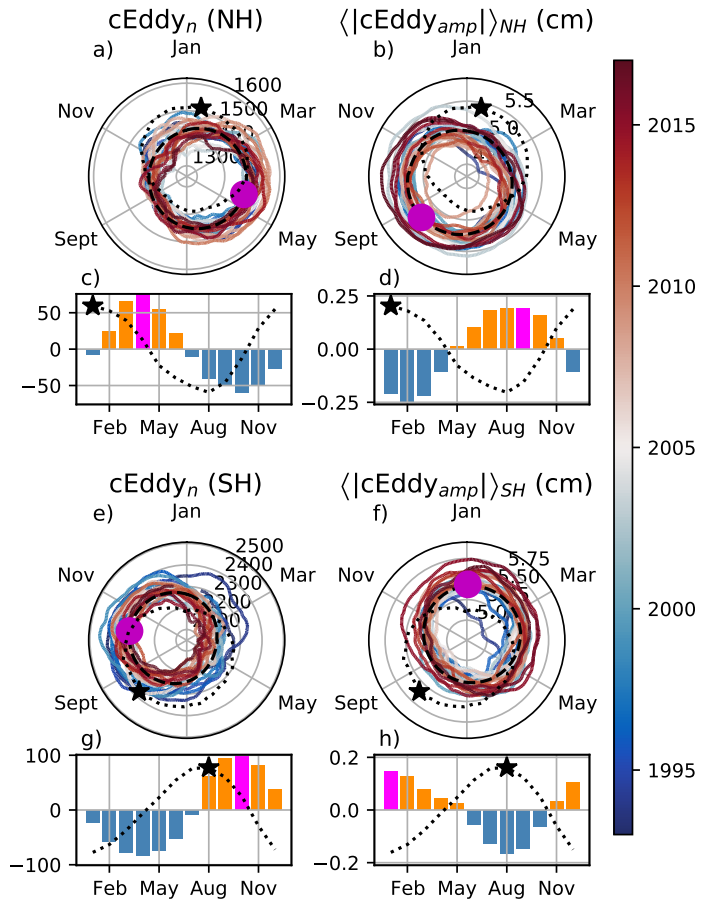
suggests that wind driven baroclinic instabilities generate small coherent eddies early in the season, which then merge and grow to become larger in diameter and amplitude, and thus, more energetic. This process is likely associated with the inverse energy cascade, and suggest that this mechanism not only drives the EKE seasonality, but also may be responsible of the seasonal cycle of coherent eddies.

Long-term changes can be observed in Figure 6a,b, e, and f where growing-shrinking concentric circles over time denote an increase-decrease trend of the field. This trend is particularly evident in the Southern Hemisphere, where the number of eddies has decreased, the eddy amplitude has increased. This result is consistent with the observed trends in EKE and mesoscale EKE in the Southern Ocean (Hogg et al., 2015; Martínez-Moreno et al., 2019). The coherent eddy amplitude from positive coherent eddies and negative coherent eddies show similar seasonal cycles to the absolute eddy amplitude. The Northern Hemisphere decrease in absolute eddy amplitude is driven by a decrease of the amplitude of negative coherent eddies in the Northern Hemisphere. Meanwhile in the Southern Ocean, the increase in absolute eddy amplitude is corroborated by an strengthening of both coherent eddy polarities since the early 90s.

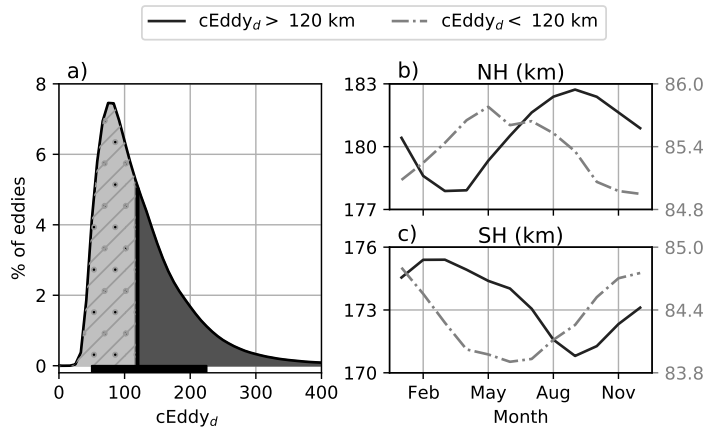
5 Trends

The results presented in Figures 4 and 6 suggest a long-term readjustment of the coherent eddy field. The long-term trends of the number of coherent eddies, absolute coherent eddy amplitude, and coherent eddy amplitude polarities are further explored in Figure 8 contrasting the MM19 and Chelton et al. (2011) methods. MM19 and Chelton's datasets show consistent spatial patterns in the trends and significance of the number of coherent eddies and the absolute coherent eddy amplitude. Several regions in the ocean, such as the Southern Ocean, North Atlantic and North Pacific, show a decrease in the number of eddies. Those same regions also have a clear increase in the absolute coherent eddy amplitude. These trends are similar to those observed in mesoscale eddy kinetic energy (Martínez-Moreno et al., 2021) and provide additional evidence of a readjustment of the mesoscale eddy field over the last 3 decades.

@Matt: What do you think? Is it important to highlight the trends we observe are different to sea level rise? Or is the next paragraph irrelevant?



333 **Figure 6.** Seasonality of the count of number of eddies ($cEddy_n$) and area weighted polarity
 334 independent coherent eddy amplitude ($\langle |cEddy_{amp}| \rangle$); Panels a and b show the time-series of the
 335 Northern Hemisphere, while panels e and f correspond to the Southern Hemisphere. Panels c
 336 and d show the seasonal cycle of the $cEddy_n$ and $\langle |cEddy|_{amp} \rangle_{NH}$ in the Northern Hemisphere,
 337 and panels g and h show the Southern Hemisphere ($cEddy_n$ and $\langle |cEddy|_{amp} \rangle_{SH}$). Dashed lines
 338 correspond to the seasonal cycle of the fields and dotted lines show the seasonal cycle of the
 339 wind magnitude smoothed over 120 days (moving average). The black and magenta markers
 340 (circle and bar) show the maximum of the seasonal cycle for the eddy property and the wind
 341 magnitude, respectively. In cyclic plots, line colors shows the year.

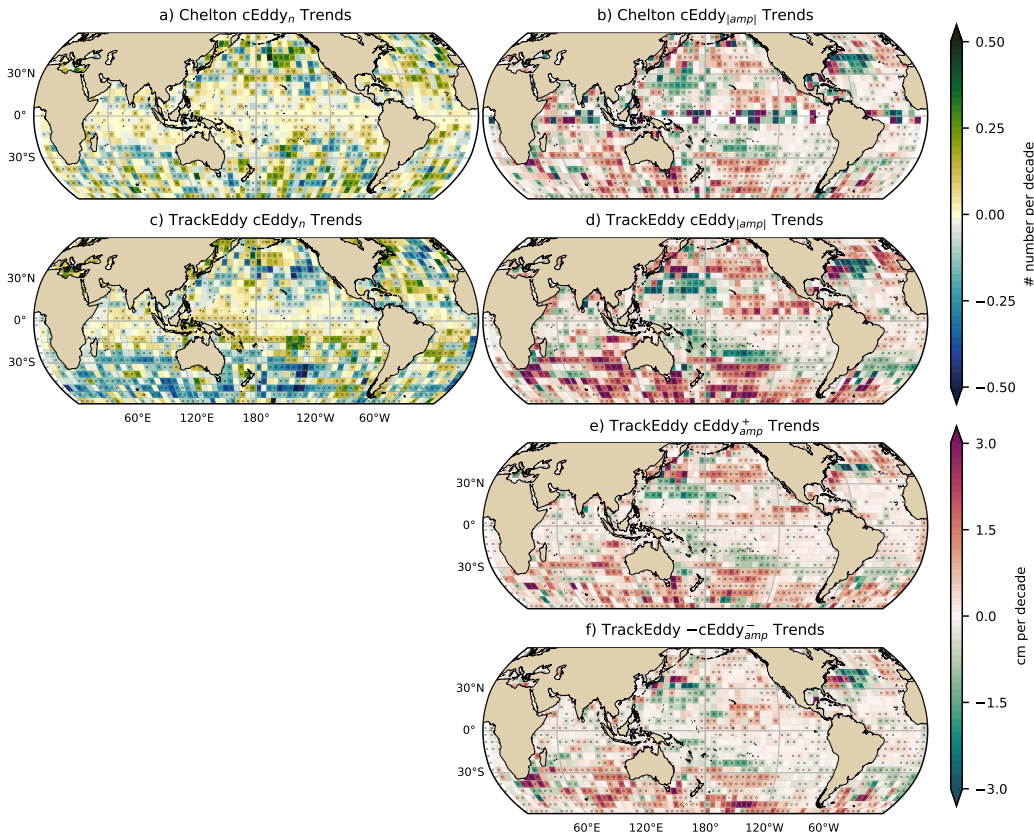


342 **Figure 7.** Distribution of the identified eddy diameter ($cEddy_d$; km) and hemispherical
 343 seasonality of the coherent eddy diameter. a) Distribution in percentage of identified eddy am-
 344 plitude, solid bar below distribution represents 90% of the identified eddies. Seasonal cycle of
 345 the eddy diameter for the b) Northern Hemisphere and c) Southern Hemisphere. Dark solid line
 346 and area corresponds to coherent eddies with diameters larger than 120 km, while light gray
 347 dash-dotted line and area shows coherent eddies with diameters smaller than 120 km.

362 The observed trends of $cEddy_{amp}$ in several oceanic regions have the same scale
 363 as sea level rise ($\sim 3\text{cm}$ per decade). By analyzing the positive and negative coherent eddy
 364 amplitude we can discard the observed trends correspond to an increase in sea level. In
 365 fact, each coherent eddy polarity has intensified in the Southern Ocean and North East
 366 Pacific and Atlantic. In other words, the amplitude of each polarity has increased over
 367 time, thus this strengthening is an intrinsic response of the coherent eddy field. Note that
 368 the negative coherent eddy amplitude dominates the global $|cEddy_{amp}|$ trends (Figure
 369 8e, f). However, different trend pattern can be observed in both positive and negative
 370 coherent eddy amplitudes in the north Atlantic and north Pacific, where the negative
 371 coherent eddy amplitude in the Western Boundary Currents appears to decrease.

379 6 Regional Climatology

380 For regions with relatively large proportions of CEKE located at boundary exten-
 381 sions and eastern currents, we investigate the seasonal and long-term variability of the
 382 coherent eddy properties. The most energetic western boundary extensions include; the
 383 Gulf Stream, the Kuroshio Current, and the Agulhas Current (Figures 9, 10, and 11).



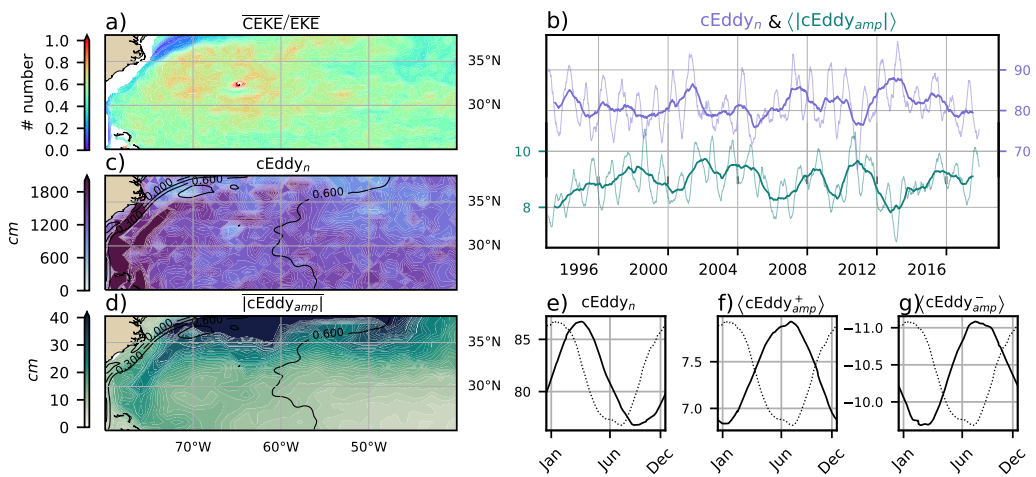
372 **Figure 8.** Trends of coherent eddy statistics. a) and b) Trends of the number of identified
 373 coherent eddies from satellite observations identified using TrackEddy, and those reported in
 374 Chelton's dataset. c) and d) Trends of the absolute value of identified coherent eddies amplitude
 375 ($cEddy_{|amp|}$) from satellite observations identified using TrackEddy, and those reported
 376 in Chelton's dataset. e) and f) Trends of eddy amplitude polarity using TrackEddy ($cEddy_{amp}^+$
 377 and $cEddy_{amp}^-$). Gray stippling shows regions that are statistically significant above the 95%
 378 confidence level.

384 Coherent eddy generation in boundary extensions occurs through baroclinic and barotropic
 385 instabilities of the mean current, thus all these regions share similar generation dynam-
 386 ics. In all these regions without exception; (i) CEKE contains 50-80% of the EKE in re-
 387 gions equatorwards from the mean western boundary extension location, (ii) the num-
 388 ber of eddies is consistently small over the mean western boundary extension location,
 389 and (iii) the eddy amplitude is larger over the mean western boundary extension loca-
 390 tion.

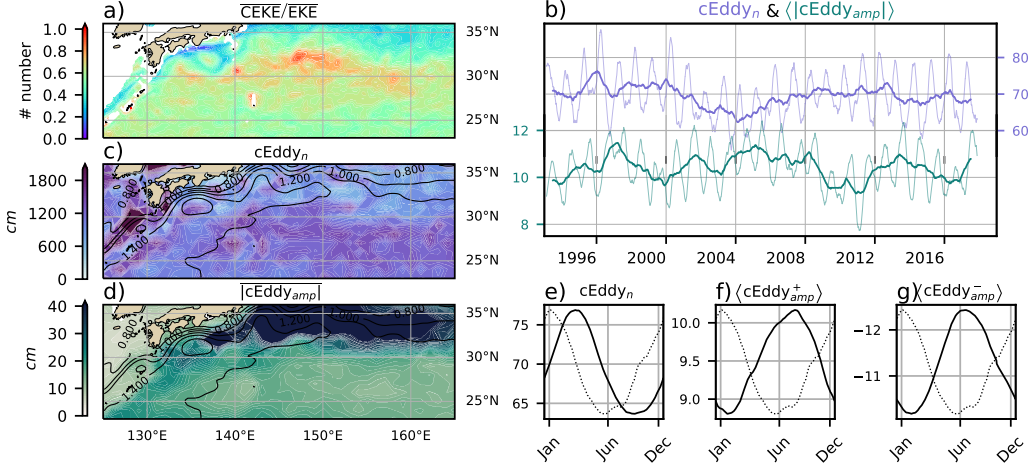
391 In the Gulf Stream, the energy ratio between CEKE and EKE is \sim 56% (Figure 9).
 392 The highest energy ratio occurs in regions with numerous eddies, collocated with regions
 393 where the largest $|cEddy_{amp}|$ gradients occurs. The time series of $cEddy_n$ and $\langle |cEddy_{amp}| \rangle$
 394 are anti-correlated (-0.52), and they display inter-annual and seasonal variability. Although
 395 Chaudhuri et al. (2009) observed a positive phase of North Atlantic Oscillation (NAO)
 396 exhibit higher EKE, due to an increase in baroclinic instabilities, thus suggesting more
 397 coherent eddies, we do not find a correlation between the $cEddy_n$ or the $\langle |cEddy_{amp}| \rangle$
 398 in the Gulf Stream and the NAO index. Similar to the signal observed in the hemispheric
 399 analysis, the eddy count seasonal cycle follows the wind maximum after \sim 3 months, while
 400 the amplitude of the coherent eddies lags by \sim 6 months.

408 The variability of the $cEddy_n$ and $\langle |cEddy_{amp}| \rangle$ in the Kuroshio Current are weakly
 409 anti-correlated (-0.41; Figure 10). However, on average 56% of the energy in the region
 410 corresponds to CEKE. As observed in the Gulf Stream, there is an important seasonal
 411 cycle in the boundary extensions, where the eddy count seasonal cycle occurs on March
 412 after \sim 3 months of the wind maximum (January). Meanwhile, the amplitude of the co-
 413 herent eddies lags by \sim 6 months (June) after the maximum wind.

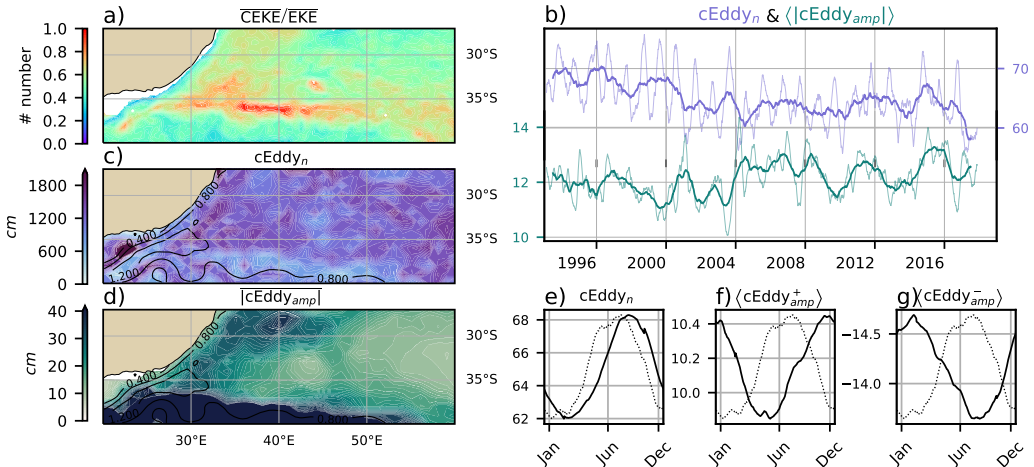
420 In the Southern Hemisphere, the strongest boundary current, the Agulhas Current
 421 shows similar behavior to its counterparts in the Northern Hemisphere (Figure 11). On
 422 average, coherent eddies in the Agulhas current contain \sim 56% of the energy, meanwhile
 423 the $cEddy_n$ seasonal peak occurs in August, while the $\langle |cEddy_{amp}| \rangle$ occurs in January-
 424 February. The seasonal lag between the winds, eddy count, and eddy amplitude in each
 425 of the western boundary current extensions is interpreted as being analogous to the ex-
 426 planation observed in Figure 6 of the lagged response of coherent eddy properties due
 427 to eddy-eddy interactions, consistent with the inverse cascade of energy.



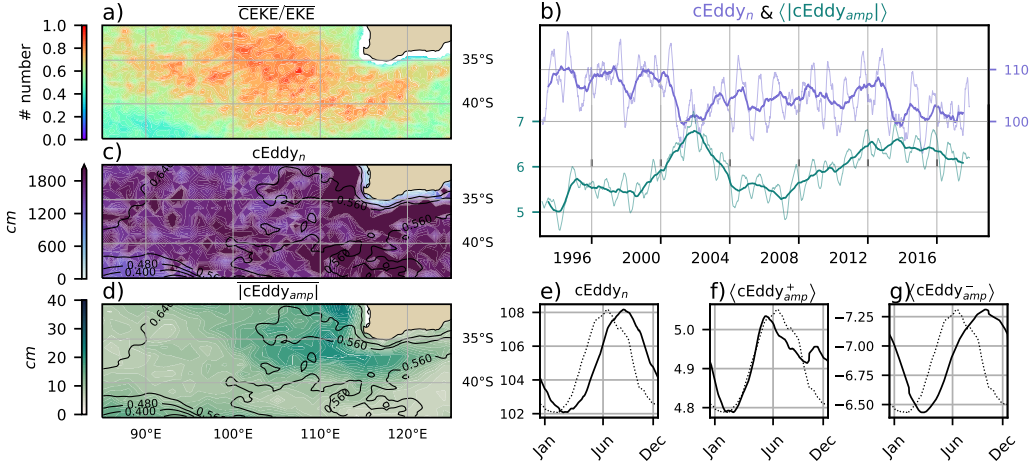
401 **Figure 9.** Climatology of the eddy field and coherent eddy field at the Gulf Stream. a) Ratio
 402 of mean coherent eddy kinetic energy (\overline{CEKE}) versus mean eddy kinetic energy (\overline{EKE}); b) Thick
 403 lines show the running average over 2 years and thin lines show the running average over 90 days
 404 of the coherent eddy number sum and the average coherent eddy amplitude; c) Map of the num-
 405 ber of eddies; d) Map of the average coherent eddy amplitude; e) Seasonal cycle of the number
 406 of eddies; f) Seasonal cycle of the positive coherent eddy amplitude, and g) Seasonal cycle of the
 407 negative coherent eddy amplitude. Contours in maps correspond to mean sea surface height (m).



414 **Figure 10.** Climatology of the eddy field and coherent eddy field at the Kuroshio extension.
 415 a) Ratio of mean coherent eddy kinetic energy ($\overline{\text{CEKE}}$) versus mean eddy kinetic energy ($\overline{\text{EKE}}$);
 416 b) Time-series of the coherent eddy number and the average coherent eddy amplitude; c) Map of
 417 the number of eddies; d) Map of the average coherent eddy amplitude; Seasonal cycle of the e)
 418 number of eddies; f) positive coherent eddy amplitude, and g) negative coherent eddy amplitude.
 419 Different lines represent the same as in Figure 9.



428 **Figure 11.** Climatology of the eddy field and coherent eddy field at the Agulhas Current. a)
 429 Ratio of mean coherent eddy kinetic energy ($\overline{\text{CEKE}}$) versus mean eddy kinetic energy ($\overline{\text{EKE}}$); b)
 430 Time-series of the coherent eddy number and the average coherent eddy amplitude; c) Map of
 431 the number of eddies; d) Map of the average coherent eddy amplitude; Seasonal cycle of the e)
 432 number of eddies; f) positive coherent eddy amplitude, and g) negative coherent eddy amplitude.
 433 Different lines represent the same as in Figure 9.



444 **Figure 12.** Climatology of the eddy field and coherent eddy field at the Leeuwin Current. a)
 445 Ratio of mean coherent eddy kinetic energy ($\overline{\text{CEKE}}$) versus mean eddy kinetic energy ($\overline{\text{EKE}}$); b)
 446 Time-series of the coherent eddy number and the average coherent eddy amplitude; c) Map of
 447 the number of eddies; d) Map of the average coherent eddy amplitude; Seasonal cycle of the e)
 448 number of eddies; f) positive coherent eddy amplitude, and g) negative coherent eddy amplitude.
 449 Different lines represent the same as in Figure 9.

434 Coherent eddies dominate the EKE field in other regions such as the Leeuwin Cur-
 435 rent (Figure 12), where the 65% of the energy is contained by coherent eddies. The Leeuwin
 436 region is not characterized by having a large EKE, however, a considerable abundance
 437 of eddies and large eddy amplitudes are observable in the region. The time-series reveal
 438 a significant increase in the $\langle |c\text{Eddy}_{amp}| \rangle$, while the $c\text{Eddy}_n$ has decreased over the last
 439 3 decades. The seasonal cycle shows that the $c\text{Eddy}_n$ peak occurs on August, 3 months
 440 after the maximum winds (June). Meanwhile, the $\langle c\text{Eddy}_{amp}^+ \rangle$ responds in synchrony
 441 to winds, and the $\langle c\text{Eddy}_{amp}^- \rangle$ is in phase with the seasonal cycle of the $c\text{Eddy}_n$. Hence,
 442 this region contrast the behavior of western boundary currents, and showcases the spa-
 443 tial variability of the seasonal cycle of coherent eddies.

450 Another region with important contributions of the coherent eddy field is the East
 451 Tropical Pacific (Tehuantepec region; Figure 13), where coherent eddies contain $\sim 58\%$
 452 of the energy. In fact, coherent eddy generation in this region is modulated by winds and
 453 coastally trapped waves which produce a strong horizontal and vertical shear (baroclinic
 454 and barotropic instabilities; Zamudio et al., 2006). Furthermore, the equatorial gener-

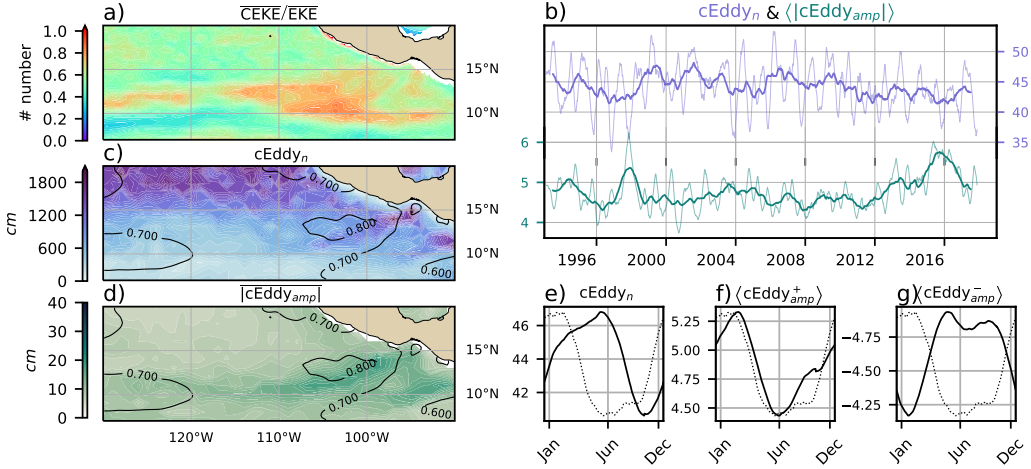


Figure 13. Climatology of the eddy field and coherent eddy field at the East Tropical Pacific.
 a) Ratio of mean coherent eddy kinetic energy ($\overline{\text{CEKE}}$) versus mean eddy kinetic energy ($\overline{\text{EKE}}$);
 b) Time-series of the coherent eddy number and the average coherent eddy amplitude; c) Map of the number of eddies; d) Map of the average coherent eddy amplitude; Seasonal cycle of the e)
 number of eddies; f) positive coherent eddy amplitude, and g) negative coherent eddy amplitude.
 Different lines represent the same as in Figure 9.

ated waves propagating along the coast have an important interannual variability observable in the $\langle |c\text{Eddy}_{amp}| \rangle$ time-series, where El Niño events are notable during 1997 and 2015 (Figure 13b). The seasonal cycle of $c\text{Eddy}_n$, $\langle c\text{Eddy}_{amp}^+ \rangle$, and $\langle c\text{Eddy}_{amp}^- \rangle$ support the idea of a coherent eddies responding to two different coherent eddy generation mechanisms; the number of eddies lags by ~ 3 months from the winds, while the $\langle c\text{Eddy}_{amp}^+ \rangle$ is in phase with the winds and the maximum of trapped waves (winter; Zamudio et al., 2006), and the $\langle c\text{Eddy}_{amp}^- \rangle$ could be a consequence of eddy-eddy interactions.

7 Discussion and Conclusions

We investigated the contribution of coherent eddies in the kinetic energy field using satellite observations. We corroborate that around half of the EKE is explained by coherent eddies. This half is concentrated in eddy-rich regions where an intensification of the eddy field has been observed (Martínez-Moreno et al., 2021). The energy contained by eddies is larger than the previous estimate of 40% by Chelton et al. (2011). Although there are differences in the identification criteria of both eddy identification methods,

475 the main cause of the difference is likely to be the lifespan and amplitude filters. These
 476 filters are widely used to track individual eddies on space and time, however, interactions
 477 between eddies in energetic regions may obscure the abundance and influence of short-
 478 lived coherent eddies. Filters are not used in this study, and indeed a lack of filters could
 479 facilitate an over-estimation of the the energy contained by coherent eddies, when mis-
 480 identifying or mis-fitting a coherent eddy. Thus, the presented estimate represents an
 481 upper limit of the energy contained by coherent eddies.

482 In addition, it should be noted that regions with first baroclinic Rossby radius of
 483 deformation smaller than 10km cannot be resolved by satellite observations. Thus, the
 484 energy contained by coherent eddies around latitudes of 60° and those near the shore
 485 are missed from this estimate, and their role in the seasonal cycle and local dynamics
 486 remains unknown . New satellite altimeter missions (SWOT) may allow estimates of the
 487 energy contained by mesoscale coherent eddies outside the tropical region and the con-
 488 tinental slope.

489 Hemisphere-wide variability indicates a strong seasonal cycle of the EKE, CEKE,
 490 and eddy properties. The seasonal cycle of the CEKE in each hemisphere occurs as a
 491 consequence of numerous small coherent eddies interacting with each other (eddy-eddy
 492 interactions) and resulting in stronger, larger and more energetic coherent eddies dur-
 493 ing summer after a few months of the yearly coherent eddy number maxima. This re-
 494 sults reveals eddy-eddy interactions and thus the transfer of energy from smaller coher-
 495 ent eddies to larger coherent eddies could explain the observed seasonal cycle of CEKE
 496 and coherent eddies properties.

497 Coherent eddy properties showcase a non-uniform long-term readjustment of the
 498 mesoscale eddy field. Overall, the eddy number has decreased globally at a significant
 499 rate of ~ 35 eddies per decade from ~ 4000 eddies identified globally on average each day.
 500 However, large proportions of the ocean show a strengthening of the mesoscale coher-
 501 ent eddy field at a rate greater than ~ 1 cm per decade. This strengthening of the co-
 502 herent eddy amplitude is attributed to an intensification of each coherent eddy polar-
 503 ity, rather than a readjustment of the coherent eddy field to sea level rise. In other words,
 504 the coherent eddy amplitude intensification is occurring in both coherent eddy polar-
 505 ities and explain a proportion of the previously observed readjustments in the eddy field
 506 to long-term changes in the ocean forcing (Hu et al., 2020; Wunsch, 2020; Martínez-Moreno

507 et al., 2021). This long-term readjustment showcases an intensification of the coherent
508 eddy field, possibly due to long-term readjustments in the ocean baroclinic and barotropic
509 instabilities, as well as the strength of the winds.

510 The reconstruction of the coherent eddies and their statistics have revealed regions
511 with important coherent eddy contributions and a distinct seasonal evolution of the co-
512 herent eddies. Western boundary extensions generate eddies through the instability of
513 the main currents and the seasonal cycle of coherent eddies, CEKE, and thus EKE could
514 be associated with an inverse energy cascade observable through lagged seasonal cycles
515 in the coherent eddy statistics. In addition, the amplitude of the seasonal cycle in the
516 boundary extensions is two times larger than any other region, thus the seasonality of
517 the coherent eddies in boundary extensions dominate the hemispheric seasonal cycle. Fur-
518 thermore, the seasonal lag of the inverse energy cascade is coupled with the presence of
519 fronts (Qiu et al., 2014), such is the case of western boundary extensions, and our re-
520 sults are consistent with the notion of baroclinic instability generating eddies and through
521 eddy-eddy interactions a lagged inverse energy cascade.

522 The use of satellite observations in this study limit our ability to quantify the im-
523 portance of the inverse energy cascade seasonality in the control of the coherent eddy
524 seasonal cycle. As mentioned above, there is robust evidence of an increase in eddy-eddy
525 interactions, however we can not discard important contributions from other processes
526 such as the seasonal cycle of forcing and instabilities, which are crucial in the genera-
527 tion of coherent eddies. Although this study can provide a descriptive response of the
528 coherent eddy field, further studies are needed to asses the role of eddy-eddy interactions
529 in our changing climate, ocean dynamics, and biogeochemical process. Furthermore, the
530 SWOT mission could allow to advance our understanding of eddy-eddy interactions and
531 the seasonal cycle of scales smaller than mesoscale, which may provide further evidence
532 of the inverse energy cascade driving the coherent eddy seasonality.

533 Acknowledgments

534 Chelton & Schlax (2013) dataset was produced by SSALTO/DUACS and distributed by
535 AVISO+ (<https://www.aviso.altimetry.fr/>) with support from CNES, developed
536 and validated in collaboration with E.Mason at IMEDEA. Global coherent eddy recon-
537 struction, coherent and non-coherent eddy kinetic energy datasets, in addition to grid-
538 ded coherent eddy tracking datasets are publicly available at (<https://doi.org/10.5281/>

539 zenodo.4646429). All analyses and figures in this manuscript are reproducible via Jupyter
 540 notebooks and instructions can be found in the Github repository CEKE_climatology
 541 (https://github.com/josuemtzmo/CEKE_climatology). Trends used the Python Pack-
 542 age xarrayMannKendall (<https://doi.org/10.5281/zenodo.4458776>). J.M.-M. was
 543 supported by the Consejo Nacional de Ciencia y Tecnología (CONACYT), Mexico fund-
 544 ing. M.H.E. was supported by the Centre for Southern Hemisphere Oceans Research (CSHOR),
 545 a joint research centre between Qingdao National Laboratory for Marine Science and Tech-
 546 nology (QNLM), Commonwealth Scientific and Industrial Research Organisation (CSIRO),
 547 University of New South Wales (UNSW), and the University of Tasmania (UTAS). Anal-
 548 yses were undertaken on the National Computational Infrastructure in Canberra, Aus-
 549 tralia, which is supported by the Australian Commonwealth Government.

550 References

- 551 Arbic, B. K., Polzin, K. L., Scott, R. B., Richman, J. G., & Shriver, J. F. (2013).
 552 On Eddy Viscosity, Energy Cascades, and the Horizontal Resolution of Gridded
 553 Satellite Altimeter Products*. *Journal of Physical Oceanography*, 43(2), 283–300.
 554 doi: 10.1175/jpo-d-11-0240.1
- 555 Ashkezari, M. D., Hill, C. N., Follett, C. N., Forget, G., & Follows, M. J. (2016).
 556 Oceanic eddy detection and lifetime forecast using machine learning methods.
 557 *Geophysical Research Letters*, 43(23). doi: 10.1002/2016gl071269
- 558 Beron-Vera, F. J., Wang, Y., Olascoaga, M. J., Goni, G. J., & Haller, G. (2013). Ob-
 559 jective Detection of Oceanic Eddies and the Agulhas Leakage. *Journal of Physical
 560 Oceanography*, 43(7), 1426–1438. doi: 10.1175/JPO-D-12-0171.1
- 561 Bouali, M., Sato, O. T., & Polito, P. S. (2017). Temporal trends in sea surface tem-
 562 perature gradients in the South Atlantic Ocean. *Remote Sensing of Environment*,
 563 194, 100–114. doi: 10.1016/j.rse.2017.03.008
- 564 Callies, J., Flierl, G., Ferrari, R., & Fox-Kemper, B. (2015). The role of mixed-layer
 565 instabilities in submesoscale turbulence. *Journal of Fluid Mechanics*, 788, 5–41.
 566 doi: 10.1017/jfm.2015.700
- 567 Cane, M. A., Clement, A. C., Kaplan, A., Kushnir, Y., Pozdnyakov, D., Seager, R.,
 568 ... Murtugudde, R. (1997). Twentieth-Century Sea Surface Temperature Trends.
 569 *Science*, 275(5302), 957–960. doi: 10.1126/science.275.5302.957
- 570 Chaudhuri, A. H., Gangopadhyay, A., & Bisagni, J. J. (2009). Interannual variabil-

- 571 ity of Gulf Stream warm-core rings in response to the North Atlantic Oscillation.
 572 *Continental Shelf Research*, *29*(7), 856–869. doi: 10.1016/j.csr.2009.01.008
- 573 Chelton, D. B., A. d. R., Schlax, M. G., Naggar, K., & Siwetz, N. (1998). Geographical variability of the first baroclinic Rossby radius of deformation. *Journal
 574 of Physical Oceanography*, *28*(3), 433–460. doi: 10.1175/1520-0485(1998)028<433:
 575 GVOTFB>2.0.CO;2
- 577 Chelton, D. B., Gaube, P., Schlax, M. G., Early, J. J., & Samelson, R. M. (2011).
 578 The influence of nonlinear mesoscale eddies on near-surface oceanic chlorophyll.
 579 *Science*, *334*(6054), 328–32. doi: 10.1126/science.1208897
- 580 Chelton, D. B., & Schlax, M. G. (2013). *Mesoscale eddies in altimeter observations
 581 of ssh*.
- 582 Chelton, D. B., Schlax, M. G., Samelson, R. M., & de Szoeke, R. A. (2007). Global
 583 observations of large oceanic eddies. *Geophysical Research Letters*, *34*(15),
 584 L15606. doi: 10.1029/2007GL030812
- 585 CMEMS. (2017). The Ssalto/Duacs altimeter products were produced and dis-
 586 tributed by the Copernicus Marine and Environment Monitoring Service. *Aviso
 587 Dataset*. Retrieved from <https://www.aviso.altimetry.fr/>
- 588 Cui, W., Wang, W., Zhang, J., & Yang, J. (2020). Identification and census statis-
 589 tics of multicore eddies based on sea surface height data in global oceans. *Acta
 590 Oceanologica Sinica*, *39*(1), 41–51. doi: 10.1007/s13131-019-1519-y
- 591 Faghmous, J. H., Frenger, I., Yao, Y., Warmka, R., Lindell, A., & Kumar, V. (2015,
 592 6). A daily global mesoscale ocean eddy dataset from satellite altimetry. *Scientific
 593 Data*, *2*, 150028 EP -. doi: 10.1038/sdata.2015.28
- 594 Ferrari, R., & Wunsch, C. (2009). Ocean Circulation Kinetic Energy: Reservoirs,
 595 Sources, and Sinks. *Annual Review of Fluid Mechanics*, *41*(1), 253–282. doi: 10
 596 .1146/annurev.fluid.40.111406.102139
- 597 Frenger, I., Gruber, N., Knutti, R., & Münnich, M. (2013). Imprint of Southern
 598 Ocean eddies on winds, clouds and rainfall. *Nature Geoscience*, *6*(8), 608 EP -.
 599 doi: 10.1038/ngeo1863
- 600 Frenger, I., Münnich, M., Gruber, N., & Knutti, R. (2015). Southern Ocean eddy
 601 phenomenology. *Journal of Geophysical Research: Oceans*, *120*(11), 7413–7449.
 602 doi: 10.1002/2015JC011047
- 603 Fu, L., Chelton, D., Le Traon, P., & Oceanography, M. R. (2010). Eddy dynamics

- 604 from satellite altimetry. *Oceanography*, 23(4), 14-25. doi: 10.2307/24860859
- 605 Gill, A., Green, J., & Simmons, A. (1974). Energy partition in the large-scale ocean
606 circulation and the production of mid-ocean eddies. *Deep Sea Res Oceanogr Abstr*,
607 21(7), 499-528. doi: 10.1016/0011-7471(74)90010-2
- 608 Hogg, A. M., & Blundell, J. R. (2006). Interdecadal variability of the southern
609 ocean. *Journal of Physical Oceanography*, 36(8), 1626-1645. doi: 10.1175/
610 JPO2934.1
- 611 Hogg, A. M., Meredith, M. P., Chambers, D. P., Abrahamsen, E. P., Hughes,
612 C. W., & Morrison, A. K. (2015). Recent trends in the Southern Ocean
613 eddy field. *Journal of Geophysical Research: Oceans*, 120(1), 257-267. doi:
614 10.1002/2014JC010470
- 615 Hu, S., Sprintall, J., Guan, C., McPhaden, M. J., Wang, F., Hu, D., & Cai,
616 W. (2020, 2). Deep-reaching acceleration of global mean ocean circula-
617 tion over the past two decades. *Science Advances*, 6(6), eaax7727. doi:
618 10.1126/sciadv.aax7727
- 619 Japan Meteorological Agency, Japan. (2013). *Jra-55: Japanese 55-year reanalysis,*
620 *daily 3-hourly and 6-hourly data.* Boulder CO: Research Data Archive at the Na-
621 tional Center for Atmospheric Research, Computational and Information Systems
622 Laboratory. Retrieved from <https://doi.org/10.5065/D6HH6H41>
- 623 Kang, D., & Curchitser, E. N. (2013). Gulf stream eddy characteristics in a high-
624 resolution ocean model. *Journal of Geophysical Research: Oceans*, 118(9), 4474-
625 4487. Retrieved from <https://agupubs.onlinelibrary.wiley.com/doi/abs/10.1002/jgrc.20318> doi: <https://doi.org/10.1002/jgrc.20318>
- 626 Kang, D., & Curchitser, E. N. (2017). On the Evaluation of Seasonal Variability of
627 the Ocean Kinetic Energy. *Geophysical Research Letters*, 47, 1675-1583. doi: 10
628 .1175/JPO-D-17-0063.1
- 629 Li, G., Cheng, L., Zhu, J., Trenberth, K. E., Mann, M. E., & Abraham, J. P. (2020).
630 Increasing ocean stratification over the past half-century. *Nature Climate Change*,
631 1-8. doi: 10.1038/s41558-020-00918-2
- 632 Martínez-Moreno, J., Hogg, A. M., England, M., Constantinou, N. C., Kiss, A. E.,
633 & Morrison, A. K. (2021). Global changes in oceanic mesoscale currents over the
634 satellite altimetry record. *Journal of Advances in Modeling Earth Systems*, 0(ja).
635 doi: 10.1029/2019MS001769

- 637 Martínez-Moreno, J., Hogg, A. M., Kiss, A. E., Constantinou, N. C., & Morrison,
638 A. K. (2019). Kinetic energy of eddy-like features from sea surface altimetry.
639 *Journal of Advances in Modeling Earth Systems*, 11(10), 3090-3105. doi:
640 10.1029/2019MS001769
- 641 Patel, R. S., Llort, J., Strutton, P. G., Phillips, H. E., Moreau, S., Pardo, P. C.,
642 & Lenton, A. (2020). The Biogeochemical Structure of Southern Ocean
643 Mesoscale Eddies. *Journal of Geophysical Research: Oceans*, 125(8). doi:
644 10.1029/2020jc016115
- 645 Pilo, G. S., Mata, M. M., & Azevedo, J. L. L. (2015). Eddy surface properties and
646 propagation at Southern Hemisphere western boundary current systems. *Ocean
647 Science*, 11(4), 629–641. doi: 10.5194/os-11-629-2015
- 648 Qiu, B. (1999). Seasonal Eddy Field Modulation of the North Pacific Subtropical
649 Counter-current: TOPEX/Poseidon Observations and Theory. *Journal of Physical
650 Oceanography*, 29(10), 2471–2486. doi: 10.1175/1520-0485(1999)029<2471:sefmot>2
651 .0.co;2
- 652 Qiu, B., & Chen, S. (2004). Seasonal Modulations in the Eddy Field of the South
653 Pacific Ocean. *Journal of Physical Oceanography*, 34(7), 1515–1527. doi: 10.1175/
654 1520-0485(2004)034<1515:smitef>2.0.co;2
- 655 Qiu, B., Chen, S., Klein, P., Sasaki, H., & Sasai, Y. (2014). Seasonal Mesoscale
656 and Submesoscale Eddy Variability along the North Pacific Subtropical Coun-
657 tercurrent. *Journal of Physical Oceanography*, 44(12), 3079–3098. doi:
658 10.1175/JPO-D-14-0071.1
- 659 Ruela, R., Sousa, M. C., deCastro, M., & Dias, J. M. (2020). Global and regional
660 evolution of sea surface temperature under climate change. *Global and Planetary
661 Change*, 190, 103190. doi: 10.1016/j.gloplacha.2020.103190
- 662 Sasaki, H., Klein, P., Qiu, B., & Sasai, Y. (2014). Impact of oceanic-scale inter-
663 actions on the seasonal modulation of ocean dynamics by the atmosphere. *Nature
664 Communications*, 5(1), 5636. doi: 10.1038/ncomms6636
- 665 Schubert, R., Schwarzkopf, F. U., Baschek, B., & Biastoch, A. (2019). Submesoscale
666 Impacts on Mesoscale Agulhas Dynamics. *Journal of Advances in Modeling Earth
667 Systems*, 11(8), 2745–2767. doi: 10.1029/2019ms001724
- 668 Siegel, D., Peterson, P., DJ, M., Maritorena, S., & Nelson, N. (2011). Bio-optical
669 footprints created by mesoscale eddies in the Sargasso Sea. *Geophysical Research*

- 670 *Letters*, 38(13), n/a-n/a. doi: 10.1029/2011GL047660
- 671 Uchida, T., Abernathey, R., & Smith, S. (2017). Seasonality of eddy kinetic energy
672 in an eddy permitting global climate model. *Ocean Modelling*, 118, 41-58. doi: 10
673 .1016/j.ocemod.2017.08.006
- 674 Wunsch, C. (2020). Is The Ocean Speeding Up? Ocean Surface Energy Trends.
675 *Journal of Physical Oceanography*, 50(11), 1–45. doi: 10.1175/jpo-d-20-0082.1
- 676 Wunsch, C., & Ferrari, R. (2004). Vertical mixing, energy, and the general circula-
677 tion of the oceans. *Annual Review of Fluid Mechanics*, 36(1), 281–314. doi: 10
678 .1146/annurev.fluid.36.050802.122121
- 679 Wyrtki, K., Magaard, L., & Hager, J. (1976). Eddy energy in the oceans. *Journal of*
680 *Geophysical Research*, 81(15), 2641-2646. doi: 10.1029/JC081i015p02641
- 681 Yue, S., & Wang, C. (2004). The Mann-Kendall Test Modified by Effective Sample
682 Size to Detect Trend in Serially Correlated Hydrological Series. *Water Resources*
683 *Management*, 18(3), 201–218. doi: 10.1023/b:warm.0000043140.61082.60
- 684 Zamudio, L., Hurlbert, H. E., Metzger, E. J., Morey, S. L., O'Brien, J. J., Tilburg,
685 C., & Zavala-Hidalgo, J. (2006). Interannual variability of Tehuantepec ed-
686 dies. *Journal of Geophysical Research: Oceans (1978–2012)*, 111(C5). doi:
687 10.1029/2005JC003182